Chinese Chemical Letters 34 (2023) 108007

Contents lists available at ScienceDirect

Chinese Chemical Letters

journal homepage: www.elsevier.com/locate/cclet

# Boosting charge separation of $BiVO_4$ photoanode modified with 2D metal-organic frameworks nanosheets for high-performance photoelectrochemical water splitting

Lina Wang[a], Zejun Liu[a], Jinming Zhang[a], Yuefa Jia[a], Jingwei Huang[b], Qiong Mei[a,c,*], Qizhao Wang[a,b,*]

[a] School of Water and Environment, Key Laboratory of Subsurface Hydrology and Ecological Effects in Arid Region of Ministry of Education, Chang'an University, Xi'an 710054, China
[b] College of Chemistry and Chemical Engineering, Northwest Normal University, Lanzhou 730070, China
[c] School of Land Engineering, Chang'an University, Xi'an 710054, China

ARTICLE INFO

*Article history:*
Received 20 July 2022
Revised 30 October 2022
Accepted 14 November 2022
Available online 17 November 2022

*Keywords:*
Photoelectrochemical
$BiVO_4$
Water splitting
Co-MOF
2D nanosheets
Charge separation

ABSTRACT

Water splitting by photoelectrochemical (PEC) processes to convert solar energy into hydrogen energy using semiconductors is regarded as one of the most ideal methods to solve the current energy crisis and has attracted widespread attention. Herein, Co-based metal-organic framework $(Co(bpdc)(H_2O)_4$ (Co-MOF) nanosheets as passivation layers were *in-situ* constructed on the surface of $BiVO_4$ films through an uncomplicated hydrothermal method (Co-MOF/$BiVO_4$). Under AM 1.5G illumination, synthesized Co-MOF/$BiVO_4$ electrode exhibited a 4-fold higher photocurrent than bare $BiVO_4$, measuring 6.0 mA/cm$^2$ at 1.23 V *vs.* RHE in 1 mol/L potassium borate electrolyte (pH 9.5) solution. Moreover, the Co-MOF/$BiVO_4$ film demonstrated a 96% charge separation efficiency, a result caused by an inhibited recombination rate of photogenerated electrons and holes by the addition of Co-MOF nanosheets. This work provides an idea for depositing inexpensive 2D Co-MOF nanosheets on the photoanode as an excellent passivation layer for solar fuel production.



The development of clean renewable energy and cost-effective large-scale energy storage conversion system has become one of the research hotspots [1–5]. Solar energy itself can be directly converted into chemical energy with photoelectrochemical (PEC), such as water splitting to form hydrogen ($H_2$), making it one of the most ideal and environmentally friendly energy production routes in the future [6,7]. So far, there are many semiconductor materials as photocatalysts for water oxidation, for instance, $WO_3$ [8,9], $BiVO_4$ [10], $Fe_2O_3$ [11], $SrTiO_3$ [12], among which $BiVO_4$ has attracted much attention because of its unique advantages. $BiVO_4$ has a suitable band gap of 2.4 eV and is an n-type photocatalytic material, which can absorb a large amount of visible light with a favorable band edge position [13–15]. Nevertheless, severe charge recombination in the bulk $BiVO_4$ films usually results in a relatively low charge separation and transfer efficiency. To tackle the aforementioned drawbacks, an effective strategy based on surface modification have been developed to retard back electron/hole recombination for improved photocurrent densities [16,17]. For example, the inhibition of carriers' recombination of $BiVO_4$ by the surface passivation effect of ferrihydrite results in an increased PEC activity of $BiVO_4$ [18]. Li *et al.* demonstrated that ZIF-8 overlayer acts as surface passivation layer, which improves the hole utilization of ZnO [19]. However, the synthesis methods of most surface passivation materials are complicated, the production time is long, and a vacuum atmosphere is required. Therefore, a simple synthesis route is desired for preparing the surface passivation photoanodes.

Metal-organic frameworks (MOFs), as a novel family of 2D materials, are considered to be an important candidate in the field of PEC water oxidation due to their high carrier mobility, simple preparation, low cost and easy low-temperature film formation [20]. MOF has been proven to be an effective modified layer for ZnO [19,21], $BiVO_4$ [22,23], and $Fe_2O_3$ [24–26] photoanodes. However, as far as we know, MOFs have not been adequately studied as passivation layers for PEC water oxidation.

Herein, the 2D Co-MOF nanosheets $(Co(bpdc)(H_2O)_4$ (bpdc = biphenyl-4,4′-dicarboxylic acid), Co-MOF) were deco-

* Corresponding authors at: School of Water and Environment, Key Laboratory of Subsurface Hydrology and Ecological Effects in Arid Region of Ministry of Education, Chang'an University, Xi'an 710054, China.
*E-mail addresses:* qiongmei@chd.edu.cn (Q. Mei), qzwang@chd.edu.cn (Q. Wang).

https://doi.org/10.1016/j.cclet.2022.108007
1001-8417/

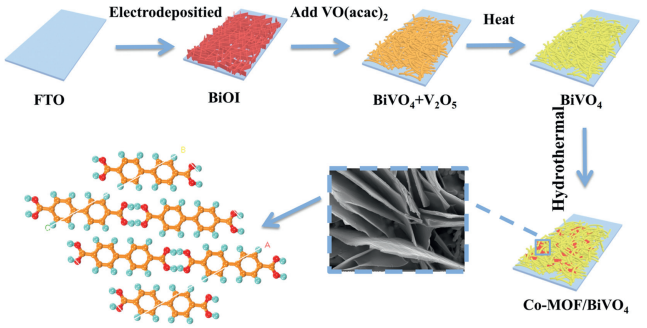


**Scheme 1.** Synthesis schematic diagram of pure $BiVO_4$, Co-MOF/$BiVO_4$ electrodes.

rated on the surface of $BiVO_4$ photoanode *via* a hydrothermal method. Meanwhile, with the introduction of Co-MOF, an active PEC water splitting reaction site is realized and the PEC water-splitting activity of $BiVO_4$ is further enhanced, which reveals that the photocurrent density can reach 6.0 mA/cm$^2$ at 1.23 V *vs.* RHE. At last, the excellent PEC performance of Co-MOF/$BiVO_4$ film is attributed to the introduction Co-MOF nanosheets passivation layer, which improves the charge separation efficiency in the pure $BiVO_4$ film.

The synthesis of Co-MOF/$BiVO_4$ consists of the following three steps: firstly, $BiVO_4$ films were synthesized by the previously reported method (Support information) [27]. Co-MOF/$BiVO_4$ electrode is synthesized by *in situ* loading Co-MOF nanosheets on $BiVO_4$ using a hydrothermal method [28]. In order to prepare Co-MOF layer, the 30 mL mixed solution contained 26 mL DMF, 2 mL water and 2 mL ethanol was prepared. Subsequently, 0.05 mmol $CoCl_2{\cdot}6H_2O$ and 0.05 mmol biphenyl-4,4′-dicarboxylic acid (bpdc) were added to the above solution under stirring. Then the above solution was transferred to a stainless steel autoclave and reacted for 8 h at 120°C. A scaffold was placed in the autoclave to allow the $BiVO_4$ electrode to stand upright in the autoclave. The dark pink precipitate was washed three times with distilled water and ethanol and dried overnight at 60°C. The steps of the fabrication of a Co-MOF/$BiVO_4$ are schematically presented in Scheme 1.

Fig. 1 provides images of the synthesized photoanodes taken with a scanning electron microscope (SEM). The pristine BiOI are comprised of uniformly deposited nanosheets that are 30–40 nm thick (Fig. 1a). According to Figs. 1b and c, the original $BiVO_4$ film has a thickness of about 2 μm and consist of small connecting ellipsoid particles. As shown in Fig. 1d, the Co-MOF nanosheets were vertically distributed throughout the whole $BiVO_4$ substrate, revealing that the Co-MOF nanosheets have been successfully introduced. In general, the resulting 2D Co-MOF nanosheets are associated with more active metal sites, which promotes more contact between the sample and oxygen, resulting in better PEC activity [29]. The corresponding analysis of the mapping image shows an even distribution of the elements Co, Bi, V and O elements in the Co-MOF/$BiVO_4$ sample (Figs. 1e–h). The microstructure of Co-MOF/$BiVO_4$ photoanode was revealed by the TEM. The image in Fig. 1i clearly shown that Co-MOF nanosheets are in close contact with $BiVO_4$. As presented in Fig. 1j, an interplanar spacing of 0.30 nm was identified, consistent with (121) lattice plane of $BiVO_4$. The interlayer lattice spacing of Co-MOF is observed to be 0.24 nm in Fig. 1j, which is consistent with previous reports [30].

The crystal structure patterns of $BiVO_4$ and Co-MOF/$BiVO_4$ photoanode are shown in Fig. 2a. In the case of $BiVO_4$ film, all peaks were indexed to the monoclinic scheelite $BiVO_4$ (JCPDS No. 14-0688) [31]. The diffraction peaks at 26.6°, 37.9°, 51.7°, 65.9° corresponded to tetragonal phase $SnO_2$ (JCPDS No. 46-1088) [32]. The XRD peaks of Co-MOF/$BiVO_4$ electrode are similar to that of $BiVO_4$

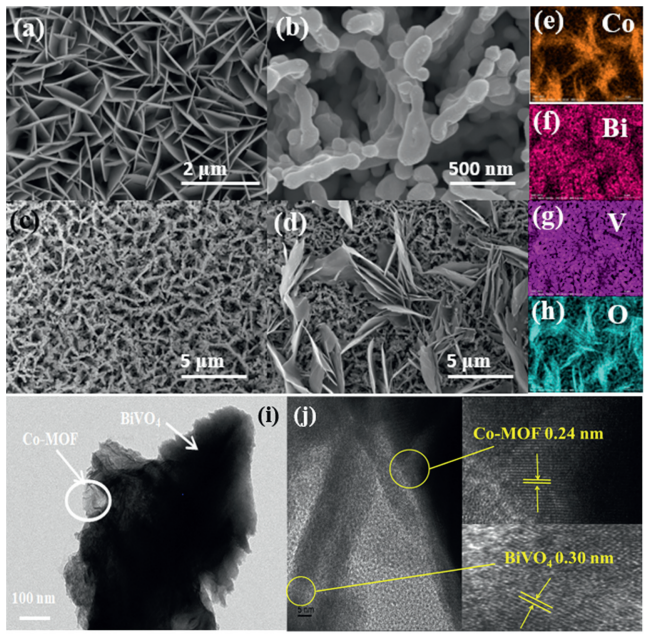


**Fig. 1.** Top-view SEM images of (a) BiOI, (b, c) $BiVO_4$, (d) Co-MOF/$BiVO_4$, (e–h) mapping, (i) TEM and (j) HR-TEM images of Co-MOF/$BiVO_4$ film.

film. However, no diffraction peaks assigned to Co-MOF can be observed, due to the small quantity of Co-MOF on the $BiVO_4$ surface. The structural components of the as-prepared $BiVO_4$, Co-MOF/$BiVO_4$ and MOF powder were further analyze *via* Fourier transform infrared spectroscopy (FT-IR). This peak is the result of the stretching vibration of C=O which is mostly caused by the presence of C=O functional groups within the bpdc bond in Fig. 2b. The antisymmetric stretching vibration peak of the carboxyl group in the ligand appeared at 1589 cm$^{-1}$ and the peak of the symmetrical stretching vibration occurred at 1367 cm$^{-1}$ [33]. The absorption peak with a wavelength of 1180 cm$^{-1}$ can be caused by the expansion and contraction vibration of C-H [34]. Furthermore, the bending vibration of C=C−H bond of benzene ring was observed at 796 cm$^{-1}$. Compared with pure MOF powder and $BiVO_4$, the FT-IR of Co-MOF/$BiVO_4$ not only showed the characteristic vibration peak of MOF ligand, but also the absorption peak of $BiVO_4$, which proved the successful modification of Co-MOF nanosheets.

Valence and surface chemical elements of $BiVO_4$ and Co-MOF/$BiVO_4$ electrode were detected by XPS. The measured spectra in Fig. S1 (Supporting information) indicated that the Bi, V, O and a small amount of Co elements are present in Co-MOF/$BiVO_4$ sample. In Fig. 2c, the peak at 781.3 eV is associated with Co $2p_{3/2}$ and 797.3 eV with Co $2p_{1/2}$, respectively [35]. Besides, the peaks of 786.4 and 802.8 eV are the signals of Co satellite peaks. In Fig. 2d, both the 159.2 and 164.5 eV peaks were observed to be associated with Bi $4f_{7/2}$ and Bi $4f_{5/2}$, respectively, which were identified as $Bi^{3+}$ in Co-MOF/$BiVO_4$. Accordingly, the binding peaks were at 516.8 eV and 524.4 eV for V $2p_{3/2}$ and V $2p_{1/2}$, respectively. (Fig. 2e). In O 1s mode from Fig. 2f, the peaks of 531.7 and 532.4 eV correspond to lattice oxygen and hydroxyl groups [36]. In conclusion, the XPS results indicated that the Co-MOF nanosheet were deposited on the $BiVO_4$ anode through *in situ* hydrothermal way.

As-fabricated anodes are shown in Fig. S2 (Supporting information) as diffuse reflectance spectra (UV-vis DRS). The $BiVO_4$ film has shown extended light absorption up to 500 nm, which is attributable to inherent bandgap energy of $BiVO_4$. After introduction of Co-MOF nanosheets on $BiVO_4$ surface, the light absorption band edge of Co-MOF/$BiVO_4$ anode exhibited a slight red shift compared to pure $BiVO_4$. The band gap of $BiVO_4$ electrode and Co-

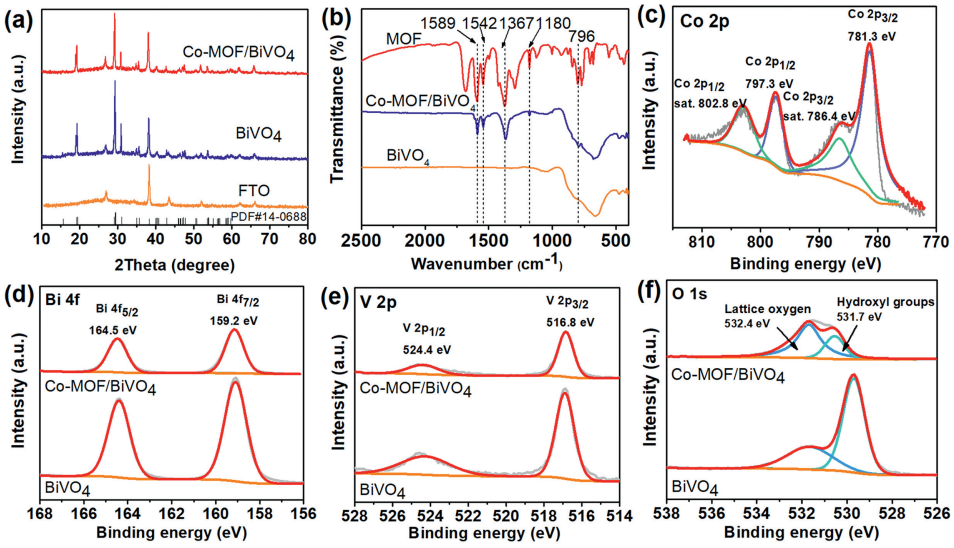


**Fig. 2.** (a) XRD analysis. (b) FT-IR patterns. High-resolution (c) Co 2p, (d) Bi 4f, (e) V 2p and (f) O 1s XPS spectra of the Co-MOF/$BiVO_4$ sample.

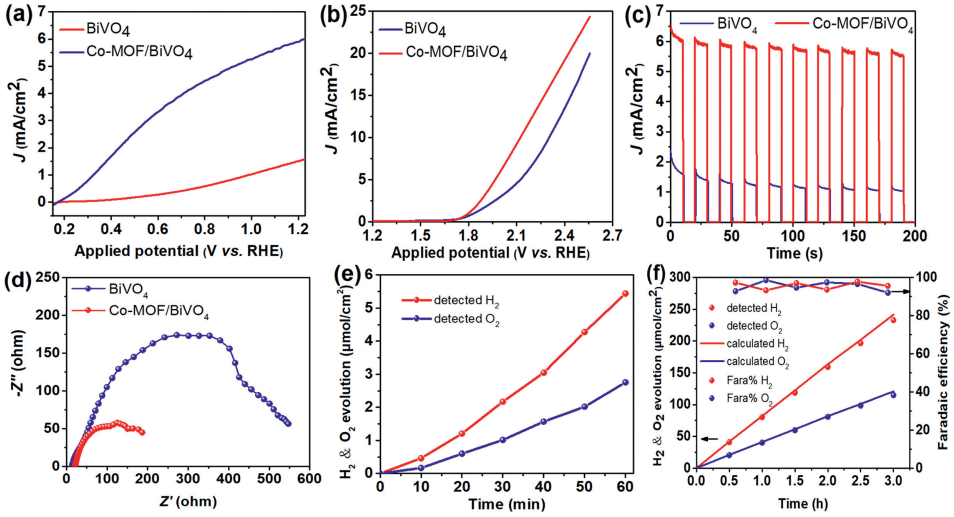


**Fig. 3.** LSV curves of $BiVO_4$, Co-MOF/$BiVO_4$ electrode with (a) and without (b) light. (c) Current-time curves of $BiVO_4$, Co-MOF/$BiVO_4$ electrode in 1 mol/L potassium borate electrolyte (pH 9.5) aqueous solution with light. (d) Electrochemical impedance spectroscopy (EIS) at 1.23 V *vs.* RHE under illumination. (e) $H_2$ and $O_2$ evolution of $BiVO_4$ and (f) Co-MOF/$BiVO_4$ films at 1.23 V *vs.* RHE and the Faradaic efficiency.

MOF/$BiVO_4$ samples were evaluated from their UV-vis DRS using the Kubelka-Munk formula in Fig. S3 (Supporting information). It is obvious that the band gap value of Co-MOF/$BiVO_4$ sample (2.38 eV) is narrower than that of $BiVO_4$ (2.43 eV), implying that Co-MOF nanosheets can slightly affect the band gap value of $BiVO_4$.

To fundamentally explain the excellent PEC water performance of Co-MOF/$BiVO_4$ sample, linear sweep voltammograms (LSV) were carried out. In order to exclude the effect of FTO on the PEC properties of other samples, the LSV test of FTO was carried out under the same conditions. As shown in the Fig. S4 (Supporting information), the photocurrent density of the FTO is almost zero, indicating that the FTO acts as a support material in the composite. To determine the optimal thickness of 2D Co-MOF nanosheets, the different concentrations of $CoCl_2{\cdot}6H_2O$ and bpdc (0.2, 0.1, 0.05 and 0.025 mmol) have been investigated. As displayed in Fig. S5 (Supporting information), the optimal loading of Co-MOF nanosheets is 0.05 mmol. As shown in Fig. 3a, the photocurrent density of $BiVO_4$ (1.5 mA/$cm^2$) at 1.23 V *vs.* RHE is low. However, the highest photocurrent density of 6.0 mA/$cm^2$ at 1.23 V *vs.* RHE is obtained for Co-MOF/$BiVO_4$ sample, obviously higher than pure $BiVO_4$, as a result of the improvement of charge carries transfer. It is reported that the higher the negative overpotential, the higher the PEC water oxidation capacity [37]. Co-MOF/$BiVO_4$ photoanode delivered a higher current density at the same potential and obtained a water splitting initial potential of *ca.* 0.18 V *vs.* RHE, negatively shifted relative to $BiVO_4$, indicating suppression of back carries recombination and improved carries migration kinetics [17]. This observation is consistent with that reported for $Al_2O_3$-passivated hematite photoanodes [37]. Interestingly, Co-MOF/$BiVO_4$ is superior to the other samples as far as we concerned (Table S1 in Supporting information). Fig. 3b compares the LSV measurements of Co-MOF/$BiVO_4$ photoanode and $BiVO_4$ film without illumination. Notably, after introducing Co-MOF nanosheets, the LSV curve of Co-MOF/$BiVO_4$ moved significantly to the negative potential direction, indicating that reduction of the reaction energy barriers is to be achieved. Besides, the chopped light irradiation of all photoanodes were determined at 0.6 V *vs.* Ag/AgCl. The photocurrent value of Co-MOF/$BiVO_4$ is higher than that of $BiVO_4$ in Fig. 3c, which means that the transmission of photogenerated electrons in Co-MOF/$BiVO_4$ is more unimpeded. To investigate the interfa-

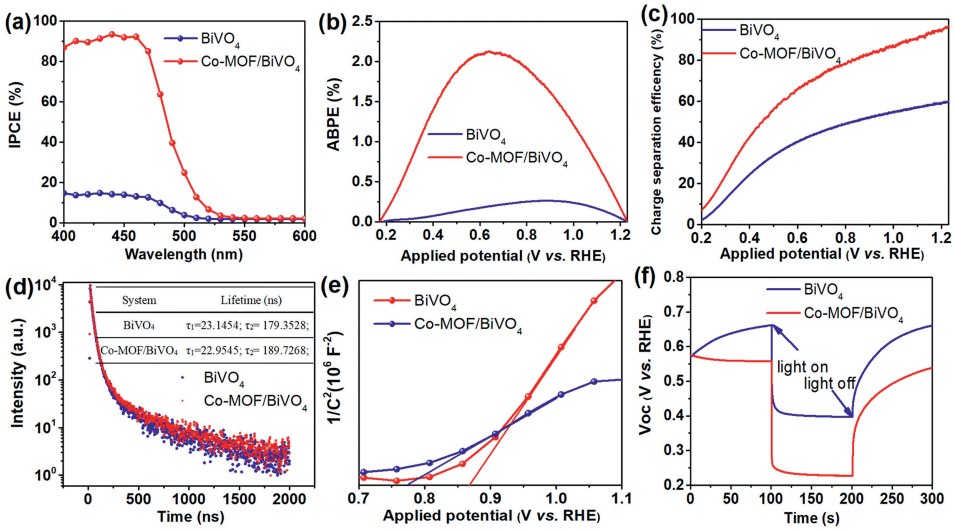


**Fig. 4.** (a) IPCE measured at 1.23 V *vs.* RHE; (b) ABPE; (c) charge separation efficiency ($\eta_{bulk}$); (d) the time-resolved PL spectra; (e) Mott-Schottky curve and (f) open-circuit photovoltage ($V_{oc}$) *vs.* time curves of the prepared $BiVO_4$, Co-MOF/$BiVO_4$ photoanodes.

cial charge separation behavior of all electrodes, a study of electrochemical impedance spectroscopy was performed, as illustrated in Fig. 3d. It is easy to distinguish two different semicircles at low frequencies and high frequencies. The latter is a characteristic of the event impedance in the bulk of the film, while the former is a characteristic of the impedance generated by the surface process [38,39]. Obviously, the semicircle of Co-MOF/$BiVO_4$ at low frequencies is much smaller than that of $BiVO_4$, indicating that Co-MOF nanosheets passivate the surface state of $BiVO_4$ then reduce electron-hole recombination in the surface state.

At 1.23 V *vs.* RHE, the PEC $H_2$ evolution activity on $BiVO_4$ alone and Co-MOF/$BiVO_4$ composite were evaluated under xenon arc lamp illumination (Figs. 3e and f). Using bare $BiVO_4$, development of $H_2$ and $O_2$ was very low, with 12 μmol $h^{-1}$ $cm^{-2}$ and 6 μmol $h^{-1}$ $cm^{-2}$, respectively, due to rapid electron and hole recombination (Fig. 3e). When a small amount of Co-MOF nanosheets is modified on the $BiVO_4$ surface in Fig. 3f, it shows a very high PEC $H_2$ and $O_2$ evolution activity of 233 μmol/$cm^2$ and 115 μmol/$cm^2$ and passed charge during the decomposition of water (Fig. S6 in Supporting information), which fully illustrates that the use of Co-MOF nanosheets to modify $BiVO_4$ is a very effective mean to improve the $BiVO_4$ PEC hydrogen production activity. The ratio of evolved $O_2$ and $H_2$ is equivalent to stoichiometric ratio of 1:2. Moreover, $H_2$ and $O_2$ have a Faraday efficiency greater than 90%. The Co-MOF/$BiVO_4$ electrode shows good reproducibility in Fig. S7 (Supporting information) with a photocurrent density of 4.8 mA/$cm^2$ at 1.23 V *vs.* RHE after PEC water oxidation reaction. It is worth noting that the Co-MOF/$BiVO_4$ photoanode exhibited excellent photocurrent and structural stability throughout the PEC water oxidation reaction test (Figs. S8–S10 in Supporting information), indicating that the introduction of the Co-MOF layer not only significantly increased the photocurrent density but also effectively contributed to the PEC stability of the $BiVO_4$ photoanode. The XRD pattern of the Co-MOF/$BiVO_4$ film shows a high match with fresh XRD and no other diffraction peaks appears, demonstrating the good stability of the Co-MOF/$BiVO_4$ photoanode (Fig. S11 in Supporting information).

The incident photon-to-current efficiency (IPCE) is also performed to measure the Co-MOF/$BiVO_4$ and $BiVO_4$ photoanodes PEC performance. From Fig. 4a, the Co-MOF/$BiVO_4$ anode achieved the highest IPCE value in the entire spectrum. Especially at 440 nm, the IPCE value was significantly increased to 93%, which is 6.2 times that of $BiVO_4$ (15% at 430 nm). According to Fig. 4b, the $BiVO_4$ photoanode has a low applied bias photon to current efficiency (ABPE) value. After modification of the $BiVO_4$ photoelectrode with the Co-MOF nanosheets, the ABPE is estimated as 2.12% at 0.64 V *vs.* RHE, corresponding to an eight-fold boost over for $BiVO_4$ (0.26% at 0.92 V *vs.* RHE). In order to reveal the mechanism of action by quantitative analysis, the charge injection efficiency ($\eta_{surface}$) of the synthetic film is provided in Fig. S12 (Supporting information). Less than 32% of the charge injection efficiency occurs at the bare $BiVO_4$ anode in the overall potential window over the entire potential range, implying that the pores generated by photons to participate in the oxidation reaction of water partially recombine with electrons instead of reaching the surface of the photoanode. However, the charge injection efficiency of Co-MOF/$BiVO_4$ photoelectrode showed significant improvement over the entire potential window, with the maximum value reaching up to 77.0% max at 1.23 V *vs.* RHE, indicating the addition of Co-MOF nanosheets greatly inhibited electron-hole recombination in $BiVO_4$. To further explore PEC behavior, the separation efficiency of the charges ($\eta_{bulk}$) was also studied in Fig. 4c. The charge separation efficiency of the Co-MOF/$BiVO_4$ photoanode was 96%, which was approximately about 1.62 times that of the $BiVO_4$ photoanode (59%), indicating that the electron-hole recombination was more severe in the original $BiVO_4$, while the Co-MOF mainly reduced the occurrence of this phenomenon. This result further demonstrated that the introduction of passivation layer of Co-MOF nanosheet can achieve efficient charge separation. To further investigate the recombination characteristics of photogenerated carriers, we tested the photoluminescence spectrum (PL) of the sample in Fig. S13 (Supporting information). The emission peak position of the Co-MOF/$BiVO_4$ anode is consistent with that of $BiVO_4$ (508 nm, Fig. S14 in Supporting information), but the emission peak intensity is reduced. Therefore, the introduction of Co-MOF nanosheets improves the photogenerated charges separation rate of $BiVO_4$ and further promotes the improvement of PEC water decomposition performance of $BiVO_4$ anode. To get a sense the critical role of charge separation efficiency in the ultimate PEC performance, time-resolved PL (TRPL) attenuation measurements of $BVO_4$ and Co-MOF/$BiVO_4$ sample were performed. Significantly, the decreased fast carrier lifetime ($\tau_1$) of Co-MOF/$BiVO_4$ implied a more effective surface charge transfer compared with that of pure $BiVO_4$ (inset Fig. 4d), which is consistent with previous reports [37,40].

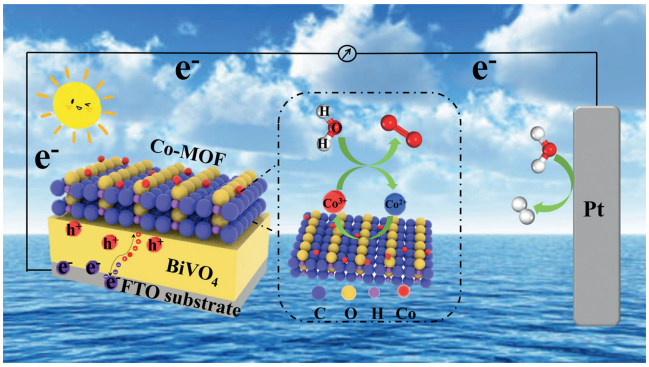


**Fig. 5.** The possible PEC hydrogen generation mechanism of Co-MOF/$BiVO_4$ photoanode.

Besides, the free exciton lifetime ($\tau_2$) in Co-MOF/$BiVO_4$ anode is increased relative to $BiVO_4$, indicating that the introduction of Co-MOF nanosheets can effectively promote the interfacial photogenerated carries separation of $BiVO_4$.

To a better comprehension, the existence mechanism of $BiVO_4$ and Co-MOF nanosheets, the Mott-Schottky of as-prepared anodes is shown in the Fig. 4e. In general, a smaller slope of graph in Fig. 4e indicates a higher density of free carriers and a higher conductivity [41]. In our case, Co-MOF/$BiVO_4$ has a lower slope than $BiVO_4$, indicating that Co-MOF nanosheets passivates the surface of $BiVO_4$ and thus reduces carriers' recombination. The addition of Co-MOF nanosheets leads to an increase in the conductivity of $BiVO_4$ and further improves the PEC water decomposition performance of $BiVO_4$, which corresponds to the result in Fig. 3d. A function of time of open circuit voltage ($V_{oc}$) has been used to analyze the electronic recombination kinetics of the prepared photoanode in 1 mol/L borate buffer electrolyte under sunlight irradiation. Fig. 4f illustrates that Co-MOF/$BiVO_4$'s $V_{oc}$ decay rate is lower than bare $BiVO_4$'s. Therefore, the lower $V_{oc}$ decay rate of Co-MOF/$BiVO_4$ provides a greater driving force for charge separation.

According to CV cycle diagram of Co-MOF/$BiVO_4$ sample in Fig. S15 (Supporting information), there is a reduction peak at *ca.* 1.6 V *vs.* RHE [42]. XPS was used to further analyze the changes in the surface structure and chemical state of Co-MOF/$BiVO_4$ after PEC water splitting testing. The $Co^{3+}$ can be observed obviously in Fig. S16 (Supporting information), indicating that the $Co^{2+}$ becomes $Co^{3+}$ oxidized *via* holes of $BiVO_4$ in part in the Co-MOF nanosheets [43]. The above experimental results indicate that $Co^{2+}/Co^{3+}$ are constantly transformed into each other in Co-MOF/$BiVO_4$ electrode. Considering the experimental results and literature reports, we discussed the possible reaction mechanism of Co-MOF/$BiVO_4$ photoanode PEC water splitting in the Fig. 5. Under irradiation, the photogenerated electrons will transfer to the Co-MOF/$BiVO_4$ surface, and further captured by the Pt electrode through the external circuit, thereby participating in the reduction of water to produce $H_2$. While the photogenerated holes tend to move to the surface of $BiVO_4$ and captured by the Co-MOF nanosheets. Subsequently, the $Co^{2+}$ is oxidized to $Co^{3+}$ by holes. Afterwards, the oxygen is produced in the process of unstable $Co^{3+}$ is reduced to $Co^{2+}$ by electrons to oxidize the interfacial $H_2O$. Moreover, the continuous conversion of $Co^{2+}$ and $Co^{3+}$ to each other provides a steady stream of active sites for water oxidation [44,45]. These processes realize the effective transfer and separation of photogenerated charges of $BiVO_4$, which is conducive to PEC water spitting. In short, the reason for this enhanced PEC performance can be associated with the synergistic effect of Co-MOF nanosheets and $BiVO_4$.

In summary, a novel passivation layer, namely 2D Co-MOF nanosheets, was *in situ* deposited on the $BiVO_4$ photoanode through a unique strategy of hydrothermal reaction to inhibit recombination rate of carriers. With a current density of 6.0 mA/$cm^2$, the resultant Co-MOF/$BiVO_4$ photoanode displayed significant improvements in PEC oxidation over the original $BiVO_4$ film at 1.23 V *vs.* RHE under AM 1.5G irradiation. Based on the optimized Co-MOF/$BiVO_4$ photoanode, 96% of charge separation efficiency is achieved under AM 1.5G irradiation at 1.23 V *vs.* RHE, indicating that the water oxidation is carried out efficiently with surface holes to improve charge separation efficiency. Moreover, the Co-MOF/$BiVO_4$ film displayed higher $H_2$ and $O_2$ evolution rates of 233 μmol/$cm^2$ and 115 μmol/$cm^2$ for PEC water spitting, about 20 times that of pure $BiVO_4$ film. The outstanding PEC performance of Co-MOF/$BiVO_4$ photoanode may be attributed that the passage of photoexcited charge carriers of $BiVO_4$ is effectively inhibited by the passivation layer of 2D Co-MOF nanosheets.

## Declaration of competing interest

The authors declare no conflict of interest.

## Acknowledgments

This work was financially supported by the National Natural Science Foundation of China (No. 52173277), the Innovative Research Team for Science and Technology of Shaanxi Province (No. 2022TD-04), the Fundamental Research Funds for the Central Universities of Chang'an University (Nos. 300102299304, 300102291403), the Natural Science Basic Research Fund of Shaanxi Province (No. 2020JZ-20).

## Supplementary materials

Supplementary material associated with this article can be found, in the online version, at doi:10.1016/j.cclet.2022.108007.

## References

[1] S. Huang, T. Ouyang, B. Zheng, et al., Angew. Chem. Int. Ed. 60 (2021) 9546–9552.
[2] S. Wu, Z. Xu, J. Zhang, et al., Sol. RRL 5 (2021) 2100668.
[3] Z. Cao, Q. Wang, H. Cheng, Chin. Chem. Lett. 32 (2021) 2617–2628.
[4] S. Wang, W.E.I. Chen, W. Zhou, et al., Energy Environ. Sci. 14 (2021) 6428–6440.
[5] Y. Chen, M. Xu, J. Wen, et al., Nat. Sustain. 4 (2021) 618–626.
[6] A. Fujishima, K. Honda, Nature 238 (1972) 37–38.
[7] X. Wang, H. Jiang, M. Zhu, et al., Chin. Chem. Lett. 34 (2023) 107683.
[8] Y. Li, Q. Mei, Z. Liu, et al., Appl. Catal. B: Environ. 304 (2022) 120995.
[9] B. Chen, Z. Zhang, M. Baek, et al., Appl. Catal. B: Environ. 237 (2018) 763–771.
[10] J. Jian, Y. Xu, X. Yang, et al., Nat. Commun. 10 (2019) 2609.
[11] Y. Wang, J. Huang, L. Wang, et al., Chin. J. Struct. Chem. 41 (2022) 2201054–2201068.
[12] Y. Zhang, Y. Li, D. Ni, et al., Adv. Funct. Mater. 29 (2019) 1902101.
[13] T. Tian, C. Dong, X. Liang, et al., J. Catal. 377 (2019) 684–691.
[14] Q. Meng, B. Zhang, L. Fan, et al., Angew. Chem. Int. Ed. 58 (2019) 19027–19033.
[15] M. Zheng, X. Cao, Y. Ding, et al., J. Catal. 363 (2018) 109–116.
[16] S. He, C. Yan, X Chen, et al., Appl. Catal. B: Environ. 276 (2020) 119138.
[17] Y. Li, Q. Wang, X. Hu, et al., Chem. Eng. J. 433 (2022) 133592.
[18] H. Yin, D. Li, X. Wang, et al., J. Phys. Chem. C 125 (2021) 8369–8375.
[19] X. Li, S. Liu, K. Fan, et al., Adv. Energy Mater. 8 (2018) 1800101.
[20] D. Xu, T. Xia, W. Fan, et al., Appl. Surf. Sci. 491 (2019) 497–504.
[21] H. Han, F. Karlicky, S. Pitchaimuthu, et al., Small 15 (2019) 1902771.
[22] W. Zhang, R. Li, X. Zhao, et al., ChemSusChem 11 (2018) 2710–2716.
[23] S. Kim, T.A. Dela Pena, S. Seo, et al., Appl. Surf. Sci. 563 (2021) 150357.
[24] X. Wei, Y. Li, H. Peng, et al., Chem. Eng. J. 355 (2019) 336–340.
[25] S. Huang, B. Zheng, Z. Tang, et al., Chem. Eng. J. 422 (2021) 130086.
[26] R. Mo, D. Han, Z. Ren, et al., Chin. Chem. Lett. 32 (2021) 3619–3622.
[27] T.W. Kim, K.S. Choi, Science 343 (2014) 990–994.
[28] M. Liu, L. Kong, X. Wang, et al., Nano Res. 14 (2021) 4680–4688.
[29] M.F.R. Samsudin, H. Ullah, R. Bashiri, et al., ACS Sustain. Chem. Eng. 8 (2020) 9393–9403.
[30] G. Chen, J. Zhang, F. Wang, et al., Chem. Eur. J. 24 (2018) 18413–18418.
[31] J. Huang, Y. Tian, Y. Wang, et al., J. Solid State Chem. 299 (2021) 122154.
[32] X. Cao, C. Xu, X. Liang, et al., Appl. Catal. B: Environ. 260 (2020) 118136.
[33] Z. Zou, T. Wang, X. Zhao, et al., ACS Catal. 9 (2019) 7356–7364.
[34] J. Huang, K. Li, L. Wang, et al., Chin. Chem. Lett. 33 (2022) 3787–3791.
[35] K. Villa, F. Novotny, J. Zelenka, et al., ACS Nano 13 (2019) 8135–8145.

[36] Y. Jia, W. Zhang, J.Y. Do, et al., Chem. Eng. J. 402 (2020) 126193.
[37] F. Le Formal, N. Tétreault, M. Cornuz, et al., Chem. Sci. 2 (2011) 737–743.
[38] M. Tayebi, B.K. Lee, Renew. Sustain. Energy Rev. 111 (2019) 332–343.
[39] M.G. Ahmed, I.E. Kretschmer, T.A. Kandiel, et al., ACS Appl. Mater. Interfaces 7 (2015) 24053–24062.
[40] K. Zhang, B. Jin, C. Park, et al., Nat. Commun. 10 (2019) 2001.
[41] H. She, P. Yue, J. Huang, et al., Chem. Eng. J. 392 (2020) 123703.
[42] M. Chhetri, S. Dey, C.N.R. Rao, ACS Energy Lett. 2 (2017) 1062–1069.
[43] X. Zhao, B. Pattengale, D. Fan, et al., ACS Energy Lett. 3 (2018) 2520–2526.
[44] F. Tang, W. Cheng, H. Su, et al., ACS Appl. Mater. Interfaces 10 (2018) 6228–6234.
[45] L. Li, S. Xiao, R. Li, et al., ACS Appl. Energy Mater. 1 (2018) 6871–6880.